IEEE Access
Multidisciplinary ⋮ Rapid Review ⋮ Open Access Journal

Received March 5, 2021, accepted March 16, 2021, date of publication March 24, 2021, date of current version April 8, 2021.

Digital Object Identifier 10.1109/ACCESS.2021.3068745

Adaptive Nonsingular Finite-Time Terminal Sliding Mode Control for Synchronous Reluctance Motor

LINJIE REN[1,2,3,4], GUOBIN LIN[4], YUANZHE ZHAO[1,2,3,4], ZHIMING LIAO[4], AND FEI PENG[5]

[1]Key Laboratory of Road and Traffic Engineering of the State Ministry of Education, Shanghai 201804, China
[2]Key Laboratory of Rail Infrastructure Durability and System Safety, Tongji University, Shanghai 201804, China
[3]College of Transportation Engineering, Tongji University, Shanghai 201804, China
[4]National Maglev Transportation Engineering Research and Development Center, Tongji University, Shanghai 201804, China
[5]College of Electrical Engineering, Qingdao University, Qingdao 266071, China

Corresponding authors: Yuanzhe Zhao (zhaoyuanzhe@tongji.edu.cn) and Zhiming Liao (liaozhiming@tongji.edu.cn)

This work was supported in part by the Project of Science and Technology Commission Shanghai Municipality under Grant 17511102302, and in part by the National Key Technology Research and Development Program of China under Grant 2016YFB1200602.

ABSTRACT Affected by the magnetic saturation effect and unmodeled dynamics, the parameters of the synchronous reluctance motor (SynRM) are highly nonlinear and time-varying. The resulting unreasonable current loop reference command severely restricts the maximum efficiency and high control performance of SynRM. Therefore, an adaptive non-singular terminal sliding mode control scheme for SynRM drive system is proposed to improve the dynamic performance and robustness. Firstly, an analytical model of flux linkage and inductance that satisfies the energy conversion mechanism is proposed to estimate the required parameters of the control system in real time. Secondly, a novel fast finite time adaptive-gain reaching law is proposed to shorten the arrival time while reducing the chatter near the sliding mode surface. Then, a non-linear disturbance observer is designed to estimate the total disturbance of the system. The asymptotic stability of the system is proved by Lyapunov's theorem. The experimental results demonstrate that the system has satisfactory dynamic performance and robustness.

INDEX TERMS Synchronous reluctance motor (SynRM), nonsingular terminal sliding mode control, fast finite time, adaptive-gain reaching law.

I. INTRODUCTION

Owing to the advantages in structural robustness, high efficiency, temperature rise capability and flux-weakening capability, synchronous reluctance motor (SynRM) has received an increasing attention in various industrial applications [1]. As a typical electromechanical energy converter with single excitation, its copper loss is generated entirely by stator current. Besides, coupled magnetic field is established completely by the stator current as well. Energy conversion inside SynRM is accomplished via the reluctance torque, which is generated by rotor in a coupled magnetic field. Thus, its distinct characteristics include high non-linearity and time-varying parameters depending on the special energy conversion mechanism. To ensure the high-efficiency operation of SynRM and minimize copper loss, rational distribution of reference currents on d-q axis is necessary. This can be achieved by implementing the maximum torque per ampere (MTPA) strategy.

There are many challenges in implementing a superior MTPA strategy for SynRM. The main obstacle is the shift of the MTPA operating point caused by the magnetic circuit nonlinear behavior. Specifically, as the motor speed or load increases, the input electric energy increases the excitation level while intensifying the coupling effect between the magnetic barrier and the magnetic bridge [2]. As a result, the increase in the excitation level causes the saturation of the magnetic circuit to increase, and the cross-coupling cancels part of the excitation energy. The MTPA operating point is deflected due to the saturation of the flux linkage and the energy transfer between the d-and q-axis. Therefore, while maintaining the excitation level, d-axis reference current must be reduced to obtain the maximum torque output. However, it is difficult to accurately assess the excitation level during motor operation. Concentratedly reflected as the time-varying characteristics of motor parameters.

The associate editor coordinating the review of this manuscript and approving it for publication was Ning Sun.

This indirectly impedes the optimal current distribution. Besides, the motor parameters are time-varying due to the highly nonlinear magnetic circuit. In addition, conventional control methods have shortcomings in simultaneously considering the optimal current distribution and control performance. Especially, in the presence of interference and dynamic uncertainty, conventional control methods cannot achieve the desired control performance.

Several research works have focused on improving the performance of SynRM drives where various methods based on advanced control strategies provide good control performance [3]–[12]. These methods can be classified into online and offline. In [3], based on the radial basis function neural network, the optimal current distribution is obtained through online evaluation of the excitation level. In [4], the method of combining backstepping control and recurrent neural network is implemented. The optimal current angle is calculated online by the recurrent neural network. In [5], an approximation integrator with compensator of gain and phase errors is proposed to estimate fluxes. In the case that the q-axis current is determined, the three-point search algorithm is implemented to obtain the optimal d-axis current reference. A Newton iteration algorithm using the inductance value calculated online was proposed in [6] to obtain the optimal current distribution. An optimization search algorithm was employed in [7] to obtain the current distribution relationship online. Furthermore, the real high-frequency pulse injection [8] and virtual high-frequency signal injection [9] based MTPA were presented through reconstructed motor torque estimates, respectively. Regarding the offline strategy, look up table (LUT)-based optimal current distribution is the most common. A high-efficiency control algorithm at maximum efficiency condition with proper current angle was presented in [10], [11]. The key to LUT to build data tables on optimal current mapping relation offline by utilizing the measured or finite element analysis (FEA) data. As a simple and easy to implement method, the price is too much storage space and limited modeling range [12]. The existing methods have a great contribution to the acquisition of the optimal current distribution relationship. However, under a certain current distribution relationship, the compensation of uncertainties and disturbances in the system is an urgent problem to be solved.

In recent years, due to its clear mathematical meaning and strong robustness, sliding mode control (SMC) has received increasing attention for the control of uncertain systems [13], [14]. In [15], a fractional-order SMC controller is proposed, improving the overall control algorithm robustness under parameter deviations. To improve the dynamic performance of permanent magnet synchronous motor (PMSM), terminal sliding mode control (TSMC) with the goal of achieving a finite settling time is proposed and applied to PMSM [16]. To overcome the singularity problem, nonsingular terminal sliding mode control (NTSMC) is proposed to design the speed controller of PMSM [17]. To further shorten the settling time, various fast terminal sliding mode control (FTSMC) [18], [19] have been proposed and successfully applied to the speed control system of PMSM. However, the global convergence of state variables in TSMC still needs to be improved. For SynRM, fast tracking of MTPA operating points under the influence of time-varying parameters and saturation is still a challenge.

The motivation to design a novel control system for SynRM is that an MTPA control guideline with unmodeled dynamic compensation based on online excitation level calculation is lacking. Therefore, an adaptive non-singular terminal sliding mode control based on nonlinear disturbance observer (ANFTSMC-NDO) system is designed to obtain and track the optimal current distribution. Through the mechanism analysis for the magnetic circuit nonlinear behavior, the flux linkage and inductance models with the d-q-axis current as the independent variable are first established, as well as the optimal current vector angle model. Then, a nonlinear controller is designed to improve the dynamic response performance. Lyapunov's stability theorem is used to prove the stability of the proposed nonlinear controller. Based on the combination of nonlinear control and the proposed optimal current angle model, the MTPA operating point is tracked. Finally, through various experiments, the robustness of the proposed control scheme is verified.

The contributions of this paper are as follows.

1) Designing an adaptive nonsingular finite-time terminal sliding mode control for a SynRM drive system that could effectively track MTPA operating points and solve the reference current distribution problem under the influence of nonlinear and time-varying parameters.

2) To solve the problem of unknown dynamics and disturbances under a specific current distribution. A nonlinear observer independent of motor parameters is designed and embedded in the adaptive terminal synovial controller. Unmodeled dynamics and disturbances are effectively compensated. Meanwhile, in the case of finite time convergence, convergence performance is adaptively adjusted. Effectively prevent chattering while accelerating the speed of convergence.

The rest of this paper is organized as follows. In section II, the non-linear flux linkage and inductance models are proposed. The shift mechanism of MTPA operating point is also analyzed. In section III, detailed ANFTSMC speed tracking control for the SynRM drive system is presented and derived. In addition, experimental results are provided to demonstrate the robustness of the proposed control system in Section IV. Finally, Section V concludes this article.

II. ELECTROMAGNETIC MODEL OF SynRM

A. CONVENTIONAL ELECTROMAGNETIC MODEL

In a d-q coordinate system rotating synchronously with the rotor, the general mathematical model considering the nonlinearity of SynRM can be expressed

as [20]:

$$\begin{aligned} u_s &= R_s i_s + \omega_e J \psi_s(i_s) + \frac{d\psi_s(i_s)}{dt} \\ \frac{d\omega_m}{dt} &= \frac{1}{\Theta}[T_e(i_s) - B\omega_m - T_L] \\ \frac{d\theta_e}{dt} &= \omega_e = p\omega_m \\ T_e(i_s) &= \frac{3}{2} p(i_s)^{\mathrm{T}} J \psi_s(i_s) \end{aligned} \tag{1}$$

where R_s denotes the stator winding resistance, $\boldsymbol{i}_s = (i_d, i_q)^{\mathrm{T}}$ denotes the stator current vector, p represents the number of pole pairs, and ω_e, ω_m represent the frequencies of motor electrical angle θ_e and mechanical angle θ_m, respectively. Θ denotes the inertia constant, B denotes the friction coefficient, $T_e(\boldsymbol{i}_s)$ denotes the electromagnetic torque, T_L is the load torque including external disturbances, and $\boldsymbol{J}$ the orthogonal rotation matrix. $\psi_s = (\psi_d, \psi_q)^{\mathrm{T}}$ is the stator flux linkage vectors. The subscripts d and q represent d- and q-axis, respectively, of which the d-axis is aligned with the direction of maximum permeability in the rotor magnetic circuit.

The coupled magnetic field in SynRM is established entirely by the stator current. Due to the particularity of the excitation circuit, the change of the flux linkage with the stator current is nonlinear. Meanwhile, the flux linkages on the d- and q-axes interact through a common magnetic circuit, which results in a redistribution of flux linkages. Such nonlinear behavior of rotor magnetic circuit is known as self-saturation and cross-saturation. Under the assumption of ignoring iron loss, the mapping relationship between flux linkages and stator current can be further expressed as [21]:

$$\begin{cases} \psi_d = \psi_d\left(i_d, i_q\right) \\ \psi_q = \psi_q\left(i_d, i_q\right) \end{cases} \tag{2}$$

To further characterize the level and variation of flux linkage for the rotor magnetic circuit, the magnetic model can be expressed with apparent inductance and incremental inductance, respectively. The apparent inductance is defined as:

$$\begin{cases} L_d^{ai}(i_d, i_q) = \dfrac{\psi_d(i_d, i_q)}{i_d} \\ L_q^{ai}(i_d, i_q) = \dfrac{\psi_q(i_d, i_q)}{i_q} \end{cases} \tag{3}$$

where superscript ai represents the apparent inductance. Meanwhile, the incremental inductance is defined as the partial derivative of flux linkage with respect to the stator current:

$$\begin{cases} L_d^{ii}(i_d, i_q) = \dfrac{\partial \psi_d(i_d, i_q)}{\partial i_d}, L_{dq}^{ii}(i_d, i_q) = \dfrac{\partial \psi_d(i_d, i_q)}{\partial i_q} \\ L_q^{ii}(i_d, i_q) = \dfrac{\partial \psi_q(i_d, i_q)}{\partial i_q}, L_{qd}^{ii}(i_d, i_q) = \dfrac{\partial \psi_q(i_d, i_q)}{\partial i_d} \end{cases} \tag{4}$$

where superscript ii represents the incremental inductance, whereas subscripts qd and dq refer to the cross-saturated incremental inductances. By substituting (2) and (3) into (1), a torque model as a function of flux linkage and apparent inductance can be obtained:

$$T_e\left(i_s\right) = \frac{3}{2} p\left(\psi_d\left(i_d, i_q\right) i_q - \psi_q\left(i_d, i_q\right) i_d\right) \tag{5}$$

B. PROPOSED ELECTROMAGNETIC MODEL

For SynRM, under the conservative field assumption, the energy balance equation can be expressed as

$$i_s^T u_s = R_s \left\| i_s \right\|^2 + \frac{dW_m}{dt} + T_e(i_s)\omega_m \tag{6}$$

where W_m denotes the magnetic energy in coupled field that varies with variation of flux linkage. For convenience, the derivative of magnetic energy can be equivalently expressed with the derivative of magnetic co-energy W_c as:

$$\frac{dW_c}{dt} = \psi_d \frac{di_d}{dt} + \psi_q \frac{di_q}{dt} \tag{7}$$

From (6), a negative correlation is present between copper loss and electromagnetic torque in the steady state, which serves as the theoretical basis for MTPA control. It is clear from formula (7) that due to the conservation of energy, the calculation result of magnetic co-energy by curve integral is irrelevant to the path integral. Accordingly, the reciprocity condition that the magnetic co-energy satisfies is:

$$\frac{\partial^2 W_c}{\partial i_d \partial i_q} = \frac{\partial^2 W_c}{\partial i_q \partial i_d} \Leftrightarrow \frac{\partial \psi_d}{\partial i_q} = \frac{\partial \psi_q}{\partial i_d} \tag{8}$$

A combination of (7) and (8) suggest that the change of stator current leads to an energy exchange between d- and q-axis. This is also the root cause of cross-saturation. Moreover, the (7) and (8) also suggest that ψ_s is an irrotational field, while W_c is the scalar potential of ψ_s. The divergence of ψ_s can be calculated by the Laplace operator ∇^2 of magnetic co-energy as:

$$\nabla^2 W_c = L_d^{ii}(i_d, i_q) + L_q^{ii}(i_d, i_q) \tag{9}$$

As expressed in (10), the magnetic co-energy satisfies Poisson's equation. Its analytical solution cannot be obtained directly, however, since the analytical form of incremental inductance is unknown. It is clear from the general solution of Poisson's equation that Gaussian terms are often contained therein. Hence, magnetic co-energy is modeled using a Gaussian-based nonlinear function. The variation in the magnetic energy caused by the current can be modeled as

$$\Delta W_c = k\left(e^{-Wi_d^2} - 1\right)\left(V_1 i_q^2 - i_q e^{-Vi_q} + \kappa_q i_q - e^{-Vi_q}\right) \tag{10}$$

Combining (7) and (10), the variation of magnetic co-energy with current can also be expressed by flux linkages as

$$\begin{cases} \psi_d(i_d, i_q) = \psi_d(i_d) - \dfrac{\partial \Delta W_c}{\partial i_d} \\ \psi_q(i_d, i_q) = \psi_q(i_q) - \dfrac{\partial \Delta W_c}{\partial i_q} \end{cases} \tag{11}$$

where $\psi_d(i_d)$ and $\psi_q(i_q)$ represent the flux linkages under the influence of self-saturation, while the second term on the right side represents the flux linkage that is influenced by cross-saturation. Under the restrictions of (8) and (11), flux linkage model based on Gaussian's function is proposed as

$$\begin{cases} \psi_d(i_d,i_q) = \alpha_d(2-e^{-\gamma_d i_d}-e^{-\gamma_{d1}i_d^2})+\beta_d i_d \\ -k\left(2Wi_d e^{-Wi_d^2}\right)\left(V_1 i_q^2 - i_q e^{-Vi_q}+\kappa_q i_q - e^{-Vi_q}\right) \\ \psi_q(i_d,i_q) = \alpha_q(2-e^{-\gamma_q i_q}-e^{-\gamma_{q1}i_q^2})+\beta_q i_q \\ -k\left(1-e^{-Wi_d^2}\right)\left(2V_1 i_q + Vi_q e^{-Vi_q}+\kappa_q\right) \\ \dfrac{\partial\psi_d(i_d,i_q)}{\partial i_q} = \dfrac{\partial\psi_q(i_d,i_q)}{\partial i_d} = -k\left(2Wi_d e^{-Wi_d^2}\right) \\ \left(2V_1 i_q + Vi_q e^{-Vi_q}+\kappa_q\right) \end{cases} \tag{12}$$

where $\{\alpha,\ \gamma,\ \beta\}$ denotes the saturation coefficient, and $\{k,\ W,\ V,\ V_1,\ \kappa_q\}$ represents the cross-saturation coefficient. Combining formulas (3) and (12), the analytical expression of apparent inductance can be derived as

$$\begin{cases} L_d^{ai}(i_d,i_q) = \dfrac{\alpha_d(2-e^{-\gamma_d i_d}-e^{-\gamma_{d1}i_d^2})}{i_d}+\beta_d \\ -k\left(2We^{-Wi_d^2}\right)\left(V_1 i_q^2 - i_q e^{-Vi_q}+\kappa_q i_q - e^{-Vi_q}\right) \\ L_q^{ai}(i_d,i_q) = \dfrac{\alpha_q(2-e^{-\gamma_q i_q}-e^{-\gamma_{q1}i_q^2})}{i_q}+\beta_q \\ -k\left(1-e^{-Wi_d^2}\right)\left(2V_1 + Ve^{-Vi_q}+\dfrac{\kappa_q}{i_q}\right) \end{cases} \tag{13}$$

Meanwhile, combining (4) and (12), the analytical expression of incremental inductance can be derived as:

$$\begin{cases} L_d^{ii}(i_d,i_q) = \alpha_d\left(\gamma_d e^{-\gamma_d i_d}+2\gamma_{d1}i_d e^{-\gamma_{d1}i_d^2}\right)+\beta_d \\ -2kW\left(e^{-Wi_d^2}-2Wi_d^2 e^{-Wi_d^2}\right) \\ \left(V_1 i_q^2 - i_q e^{-Vi_q}+\kappa_q i_q - e^{-Vi_q}\right) \\ L_q^{ii}(i_d,i_q) = \alpha_q\left(\gamma_q e^{-\gamma_q i_q}+2\gamma_{q1}i_q e^{-\gamma_{q1}i_q^2}\right)+\beta_q \\ -k\left(1-e^{-Wi_d^2}\right)\left(2V_1 + Ve^{-Vi_q}-V^2 i_q e^{-Vi_q}\right) \\ L_{dq}^{ii}(i_d,i_q) = L_{qd}^{inc}(i_d,i_q) = -k\left(2Wi_d e^{-Wi_d^2}\right) \\ \left(2V_1 i_q + Vi_q e^{-Vi_q}+\kappa_q\right) \end{cases} \tag{14}$$

C. EFFECT OF MAGNETIC CIRCUIT NONLINEARITY ON MTPA

The conventional MTPA operating point is obtained under the premise that the apparent inductance and stator resistance are constant. Accordingly, the maximum torque condition is [22]:

$$\left.\frac{dT_e}{d\gamma}\right|_{\substack{I_s=const \\ L_d^{ai}-L_q^{ai}=const}} = \frac{3}{2}pI_s^2\left(L_d^{ai}-L_q^{ai}\right)\cos(2\gamma)=0 \tag{15}$$

where γ denotes the current angle. Influenced by the magnetic circuit nonlinear behavior, the flux linkages and inductances are functions of the stator current. From (5), the derivative of torque with respect to the current angle is:

$$\frac{dT_e}{d\gamma} = \frac{3}{2}p\left[\frac{d\psi_d}{d\gamma}i_q+\frac{di_q}{d\gamma}\psi_d-\frac{d\psi_q}{d\gamma}i_d-\frac{di_d}{d\gamma}\psi_q\right] \tag{16}$$

According to (2), the derivative of stator flux linkages with respect to the current angle is:

$$\begin{cases} \dfrac{d\psi_d}{d\gamma} = \dfrac{\partial\psi_d}{\partial i_d}\dfrac{di_d}{d\gamma}+\dfrac{\partial\psi_d}{\partial i_q}\dfrac{di_q}{d\gamma} \\ \dfrac{d\psi_q}{d\gamma} = \dfrac{\partial\psi_q}{\partial i_d}\dfrac{di_d}{d\gamma}+\dfrac{\partial\psi_q}{\partial i_q}\dfrac{di_q}{d\gamma} \end{cases} \tag{17}$$

At given current and amplitude, the derivative of d-q axis current with respect to the current angle is:

$$\begin{cases} \dfrac{di_d}{d\gamma} = \dfrac{dI_s\cos(\gamma)}{d\gamma} = -i_q \\ \dfrac{di_q}{d\gamma} = \dfrac{dI_s\sin(\gamma)}{d\gamma} = i_d \end{cases} \tag{18}$$

Combining (4), (16), (17) and (18) yields the derivative of torque with respect to the current angle as:

$$\begin{aligned} \frac{dT_e}{d\gamma} &= \frac{3}{4}pI_s^2\left(L_d^{ai}-L_q^{ai}\right)\cos(2\gamma) \\ &\quad +\frac{3}{4}pI_s^2\left[\begin{array}{c}\left(L_d^{ai}-L_q^{ii}\right)+\left(L_q^{ai}-L_d^{ii}\right) \\ +\left(L_d^{ii}-L_q^{ii}\right)\cos(2\gamma)+2L_{dq}^{ii}\sin(2\gamma)\end{array}\right] \end{aligned} \tag{19}$$

$$\left.\frac{dT_e}{d\gamma}\right|_{\gamma=\gamma^{\text{opt}}} = 0 \tag{20}$$

where γ^{opt} is the optimal current angle. Comparing (15) and (19), it can be observed that the variations of the flux linkages are the main factor for the deviation of the MTPA operating point. As the excitation level increases, γ^{opt} will gradually increase [23], [24].

III. PROPOSED CONTROL SYSTEM

In order to achieve the current minimizing and improve transient response, an ANFTSMC-NDO speed tracking control is proposed for the SynRM drive system. The control block diagram of the proposed system is shown in Fig. 1, which mainly includes the speed tracking, current regulators, optimal current angle estimator and parameters estimator.

A. PROBLEM FORMULATION

Under the determined d-q axis current distribution relationship, the dynamic model of SynRM is expressed as

$$\dot{\omega}_m = -\frac{B}{\Theta}\omega_m+\frac{3p}{4\Theta}I_s^{*2}\left(L_d^{ai*}-L_q^{ai*}\right)\sin\left(2\gamma^{*\text{opt}}\right)-\frac{1}{\Theta}T_L \tag{21}$$

The superscript with $*$ represents the reference value. Due to the unknown or partly known physical quantities like external disturbance, friction coefficient, inertia constant and load in the actual control system, unmodeled dynamics are present in (21). Besides, affected by temperature variation

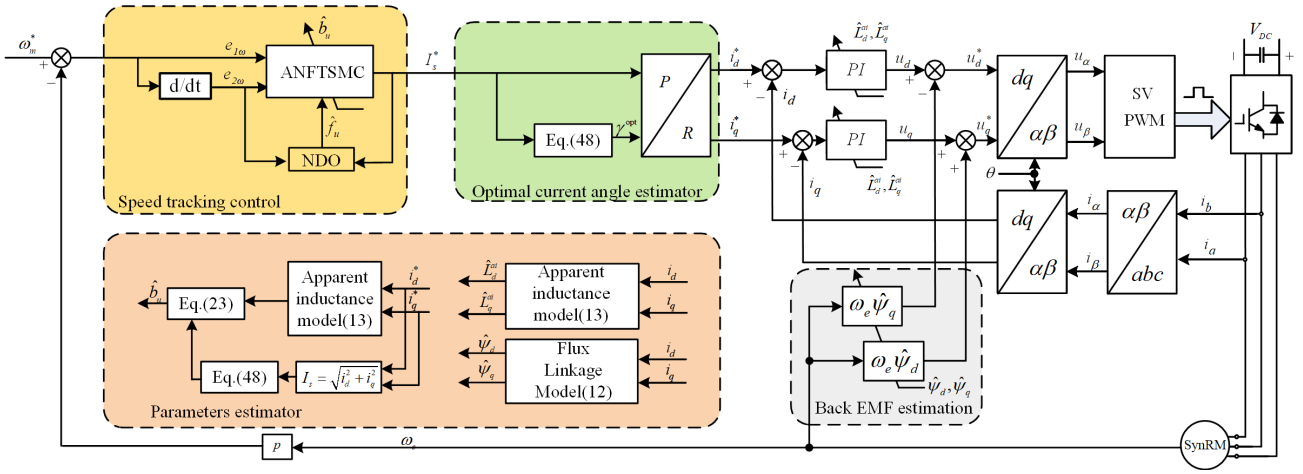

FIGURE 1. Control block diagram of ANFTSMC system.

and data fitting accuracy, there always exists an error between the apparent inductance model and the actual apparent inductance of SynRM. On these bases, a dynamic equation that considers unmodeled dynamics and parameter perturbation can be represented as:

$$\begin{aligned}\dot{\omega}_m &= -\left(a_u + \Delta a_u\right)\omega_m + \left(b_u + \Delta b_u\right)U^* - \left(c_u + \Delta c_u\right)T_L \\ &= -a_u\omega_m - b_u U^* - f \end{aligned} \tag{22}$$

The coefficient in (22) is defined as:

$$\begin{cases} u^* = I_s^{*2} \\ a_u = \dfrac{B}{\Theta} \\ b_u = \dfrac{3p}{4\Theta}\left(L_d^{ai*} - L_q^{ai*}\right)\sin\left(2\gamma^{\text{opt}}\right) \\ c_u = \dfrac{1}{\Theta} \\ f = \Delta a_u\omega_m + \Delta b_u u^* + \left(b_u + \Delta b_u\right)T_L, |f| \le F \end{cases} \tag{23}$$

where U^* denotes the square of the reference current vector amplitude, and Δb_u represents the parameter perturbation under the combined action of inertia constant, apparent inductance model error and optimal current angle fitting error. f is defined as the total disturbance of the system, which is assumed bounded, and F_b is a positive constant.

The speed tracking error and its derivative are defined as:

$$\begin{cases} e_\omega = \omega_m^* - \omega_m \\ \dot{e}_\omega = \dot{\omega}_m^* - \dot{\omega}_m \end{cases} \tag{24}$$

where ω_m^* represents the reference speed. Derivation of (24) by combining (22) yields a dynamic equation as:

$$\begin{cases} \dot{e}_\omega = \dot{\omega}_m^* - \dot{\omega}_m = \dot{\omega}_m^* + a_u\omega_m - b_u u^* + f \\ \ddot{e}_\omega = \ddot{\omega}_m^* - \ddot{\omega}_m = \ddot{\omega}_m^* - a_u\dot{e}_\omega + a_u\dot{\omega}_m^* - b_u\dot{u}^* + \dot{f} \end{cases} \tag{25}$$

where

$$\dot{f} = \Delta a_u\dot{\omega}_m + \Delta b_u\dot{u}^* + \left(b_u + \Delta b_u\right)\dot{T}_L$$

Rearrangement of (25) by taking e_ω and $\dot{e}_\omega$ as the state variables x_1, x_2 gives

$$\begin{cases} \dot{x}_1 = x_2 \\ \dot{x}_2 = -a_u x_2 - b_u\dot{u}^* + f_u \end{cases} \tag{26}$$

where

$$f_u = \ddot{\omega}_m^* + a_u\dot{\omega}_m^* + \dot{f}$$

where f_u represents the total disturbance of speed error system and $|f_u| \le F_b$. As in (26), the speed error dynamic system is a typical second-order system with unmodeled dynamics. Accordingly, the MTPA operating point tracking problem is transformed into the stabilization problem of the speed error dynamic system (26).

B. DESIGN OF AERL

The traditional exponential reaching law (TERL) [25] has the defect of poor convergence performance under different state variables [26], [27]. Besides, there are problems such as banded switching surface, chattering near the origin and insufficient reaching speed. Considering the rapidity of the exponential arrival law when it is far away from the sliding surface and the smoothness when the terminal attractor [28] $|s|^\alpha\, sgn(s)$ is close to the sliding surface, an adaptive-gain reaching law, named AERL, is proposed as

$$\dot{s} = -k_1\left(1 + \varepsilon\|x\|\right)s - \frac{k_2}{1 + \varepsilon\|x\|}|s|^\alpha\,\text{sgn}(s) \tag{27}$$

where $\|x\|$ denotes the norm of a state variable, k_1, k_2, $\varepsilon > 0, 0 < \alpha < 1$, and $sgn(\cdot)$ represents symbolic function.

According to (27), the adaptive-gain exponential reaching law $-k_1\left(1 + \varepsilon\|x\|\right)s$ and the adaptive-gain terminal attractor $-\frac{k_2}{1+\varepsilon\|x\|}|s|^\alpha\, sgn(s)$ regulate the convergence speed at different stages away from and close to the system equilibrium point, respectively. The gain variations of the two are in opposite directions. When the system state is far from the sliding surface, $\|x\|$ satisfies $\|x\| \gg 1$, thus

$$\begin{aligned} k_1\left(1 + \varepsilon\|x\|\right) &\gg k_1 \\ \frac{k_2}{1 + \varepsilon\|x\|} &\ll k_2 \end{aligned} \tag{28}$$

(28) shows that the proposed AERL convergence speed is much greater than TERL. When the system state is close to the sliding surface, $|s|$ satisfies $|s| < 1$, thus

$$\frac{k_2}{1+\varepsilon\|x\|}|s|^{\alpha} < k_2 \tag{29}$$

(29) indicates that the proposed AERL is smoother when approaching the sliding surface.

When the system state is infinitely close to zero, the proposed AERL degenerates to a fixed parameter reaching law with only smoothing effect:

$$\dot{s} = -k_1 s - k_2 |s|^{\alpha} \operatorname{sgn}(s) \tag{30}$$

Particularly, if $\alpha = 1$, (30) degenerates to TERL. Therefore, TERL is a special case of AERL.

Theorem1: For the initial state determined sliding surface, under the reaching law (27), the time from the initial state to the sliding surface is finite.

Proof: Letting the initial value of sliding surface be $s(0) = \tau > 0$, the general solution of (27) can be expressed as

$$s^{1-\alpha} = Ce^{-(1-\alpha)k_1(1+\varepsilon\|x\|)t} - \frac{k_2}{k_1(1+\varepsilon\|x\|)^2} \tag{31}$$

where

$$C = s(0)^{(1-\alpha)} + k_2 \Big/ k_1(1+\varepsilon\|x\|)^2$$

Thus, the time from the initial state to the system equilibrium state can be expressed as

$$t_r = \frac{1}{k_1(1-\alpha)} \ln\left(1 + \frac{k_1 |s(0)|^{1-\alpha}}{k_2}\right) \tag{32}$$

It is clear from (32) that at given coefficient and initial value, the time taken for the system state to converge to the origin after reaching the sliding surface is finite.

C. ANFTSMC-NDO

For ANFTSMC, its design goals are to overcome the parameter perturbation and disturbances, as well as to improve the system robustness while tracking the speed reference command. To further improve the dynamic response performance, we propose a nonsingular terminal sliding mode control strategy with AERL.

For system (26), the sliding surface is selected as:

$$s = x_1 + \frac{1}{\beta} x_2^{p/q} \tag{33}$$

where $\beta > 0$, and $p, q (p > q)$ are positive odd numbers and satisfy $1 < p/q < 2$.

Theorem2: For system (26), the sliding surface (33) is selected. Under the following control law, the system state on the sliding surface will converge to zero in a finite time.

$$\dot{u}^* = \frac{1}{b_u}\begin{bmatrix} -a_u x_2 + \beta \dfrac{q}{p} x_2^{2-p/q} + D\operatorname{sgn}(s) \\ +k_1(1+\varepsilon\|x\|)s + \dfrac{k_2}{1+\varepsilon\|x\|}|s|^{\alpha}\operatorname{sgn}(s) \end{bmatrix} \tag{34}$$

where $\beta > 0$, $D > 0$ and $p, q (p > q)$ are positive odd numbers and satisfy $1 < p/q < 2$.

Proof: To prove the stability of the proposed control method, the Lyapunov function is selected:

$$V = s^2 \Big/ 2 \tag{35}$$

Derivation and rearrangement are performed in the light of Lyapunov stability theory by combining (34) to give:

$$\begin{aligned} \dot{V} &= s\dot{s} \\ &= s\left(x_2 + \frac{1}{\beta}\frac{p}{q} x_2^{p/q-1}\dot{x}_2\right) \\ &= \frac{1}{\beta}\frac{p}{q} x_2^{p/q-1}\left[s\left[f_u - D\operatorname{sgn}(s)\right] - k_1(1+\varepsilon\|x\|)s^2 \right. \\ &\quad \left. - \frac{k_2}{1+\varepsilon\|x\|}|s|^{\alpha+1}\right] \end{aligned} \tag{36}$$

(36) Owing to $1 < p/q < 2$, that is $0 < p/q\text{-}1 < 1$. Because $\beta > 0$, and $p, q (p > q)$ are positive odd numbers, thus

$$\frac{1}{\beta}\frac{p}{q} x_2^{p/q-1} > 0, \quad x_2 \neq 0 \tag{37}$$

Thus

$$\dot{V} \le -k_1(1+\varepsilon\|x\|)s^2 - \frac{k_2}{1+\varepsilon\|x\|}|s|^{\alpha+1} \le 0 \tag{38}$$

When $x_2 \neq 0$, the controller satisfies the Lyapunov stability criterion, and the system will reach the sliding surface in finite time.

When $x_2 = 0$, (34) is substituted into (26) to get:

$$\dot{x}_2 = f_u - D\operatorname{sgn}(s) - k_1(1+\varepsilon\|x\|)s - \frac{k_2}{1+\varepsilon\|x\|}|s|^{\alpha}\operatorname{sgn}(s) \tag{39}$$

According to (39), $\dot{x}_2$ satisfies:

$$\begin{aligned} \dot{x}_2 &\ge \frac{k_2}{1+\varepsilon\|x\|}|s|^{\alpha}, \quad s < 0 \\ \dot{x}_2 &\le -\frac{k_2}{1+\varepsilon\|x\|}|s|^{\alpha}, \quad s > 0 \end{aligned} \tag{40}$$

that is, x_2 quickly decreases to negative when $s > 0$ and quickly increases to positive when $s < 0$. Therefore, when $x_2 = 0$, $s = 0$ can achieve $s = 0$ in a finite time.

In order to compensate for the internal and external disturbances present in the system by the control law (34), estimation of f_u in the system (26) is necessary, to this end, a nonlinear disturbance observer (NDO) is designed as:

$$\begin{cases} \hat{f}_u = z_1 + \zeta x_2 \\ \dot{z}_1 = -\zeta z_1 - \zeta\left(-a_u x_2 - b_u \dot{u}^* + \zeta x_2\right) \end{cases} \tag{41}$$

where $\hat{f}_u$ denotes the estimated total disturbance, z_2 denotes the internal state of NDO, and ζ represents the parameter to be designed. If $\dot{f}_u \approx 0$, the estimated error of NDO is asymptotically stable, and a positive real number ξ can always be found when the observer energy function is selected as $V_0 = e_{ob}^2/2$, such that $\dot{V}_0 < -\xi e_{ob}^2$ [29]. By defining the upper bound of

observation error as $\delta_{ob} > 0$, the NDO-based ANFTSMC can be derived through (34) combined with (41) as:

$$\dot{u}^* = \frac{1}{b_u}\begin{bmatrix} -a_u x_2 + \beta \frac{q}{p} x_2^{2-p/q} + \hat{f}_u + \\ k_1 (1+\varepsilon |x|) s + \left(\frac{k_2}{1+\varepsilon |x|} |s|^{\alpha} + e_{max} \right) \mathrm{sgn}(s) \end{bmatrix} \tag{42}$$

where e_{max} denotes the maximum estimation error of NDO. Thus, the Lyapunov function of closed-loop system with NDO can be defined as:

$$V_s = V_0 + V = \frac{e_{ob}^2}{2} + \frac{s^2}{2} > 0 \tag{43}$$

The time derivative of equation (43) is obtained:

$$\dot{V}_s = \dot{V}_0 + \dot{V} \tag{44}$$

In the closed-loop system, (36) can be rewritten as

$$\dot{V} = \frac{1}{\beta}\frac{p}{q} x_2^{p/q-1} \times \left(-k_1 (1+\varepsilon \|x\|) s^2 - \frac{k_2}{1+\varepsilon \|x\|} |s|^{\alpha+1} - \delta_{ob} |s| + s e_{ob} \right) \tag{45}$$

Substituting $\dot{V}_0 < -\xi e_{ob}^2$ and (45) into (37) yields:

$$\dot{V}_s \le \frac{1}{\beta}\frac{p}{q} x_2^{p/q-1} \times \left(-\left(k_1 (1+\varepsilon |x|) - \frac{1}{2} \right) s^2 - \frac{k_2}{1+\varepsilon |x|} |s|^{\alpha+1} \right) - \xi e_{ob}^2 \tag{46}$$

As shown in (46), when $k_1 > \frac{1}{2}$, $\dot{V}_s \le 0$ holds. (46) also suggests that in the scenario where the estimated total disturbance $\hat{f}_u$ of speed error system is obtained using NDO (41), the ANFTSMC can make the speed tracking error approach zero in a finite time by selecting the appropriate parameters.

Therefore, from (41) and (42), the reference current amplitude of the ANFTSMC-NDO control system can be expressed as

$$I_s^* = \sqrt{\int_0^t \dot{u}^* dt} = \sqrt{\int_0^t \left(\frac{1}{b_u} \begin{pmatrix} -a_u \hat{\dot{e}}_\omega + \beta \frac{q}{p} \hat{\dot{e}}_\omega^{2-p/q} + \hat{f}_u \\ +k_1 \left(1 + \varepsilon \left| e_\omega^2 + \hat{\dot{e}}_\omega^2 \right| \right) s \\ + \left(\frac{k_2}{1+\varepsilon \left| e_\omega^2 + \hat{\dot{e}}_\omega^2 \right|} |s|^{\alpha} + e_{max} \right) \mathrm{sgn}(s) \end{pmatrix} \right) dt} \tag{47}$$

In view of the accurate modeling of flux linkages, inductance and optimal current angle that takes the nonlinearity of magnetic circuit into consideration, the motor and control parameters required by the minimum copper loss control system can be calculated online merely by the present sampled current value. Based on real-time parameter calculations, the ANFTSMC-NDO compensates for unmodeled dynamics and parameter perturbation, and determines the set current amplitude I_s^*. The input of current loop is determined according to the set current amplitude output by ANFTSMC-NDO and the optimal current angle model. In addition, the decoupling of current controller is also accomplished based on the online calculation of nonlinear flux linkages.

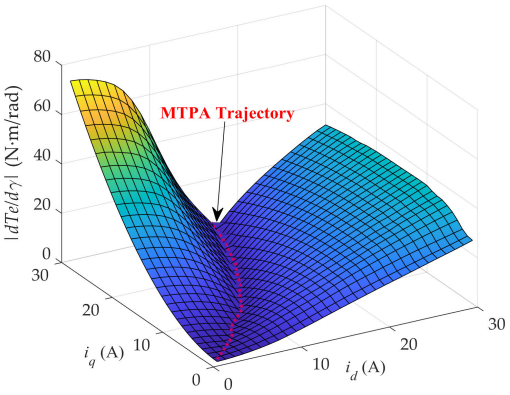

FIGURE 2. The derivative of torque with respect to the current angle at a given current amplitude.

D. OPTIMAL CURRENT ANGLE ESTIMATOR

As revealed by the comparison between (15) and (20), magnetic circuit nonlinear behaviors lead to a change in MTPA operating point. Without considering the effect of nonlinear behavior, the apparent inductance is equal to the incremental inductance, and the expressions for (15) and (20) are identical. That is, (15) is a special case of (20) when SynRM is not saturated. As shown in Fig. 2, the relationship between torque and current angle can be expressed more intuitively after incorporating the FEA results into (19) and (20).

It can be observed in Fig. 2 that the current amplitude and the optimal angle have a mapping relationship. Influenced by the nonlinear magnetic behavior, the analytical form of optimal current angle cannot be derived from (20). The relationship between stator current amplitude and optimal current angle is obtained through polynomial fitting by utilizing the data at the lowest point of curved surface in Fig.2. The fitting results are as follows:

$$\gamma^{\mathrm{opt}} = -0.00046 I_s^3 + 0.02767 I_s^2 + 0.02077 I_s + 45 \tag{48}$$

where γ^{opt} denotes the optimal current angle corresponding to a given current amplitude I_s.

E. PARAMETERS ESTIMATOR

In the ANFTSMC-NDO system, the input parameters are calculated in real time based on (13) and (14). To this end, FEA for the tested 2-kw prototype is performed. Fig. 3 depicts the nonlinear flux linkages obtained based on the FEA results.

As shown in Fig.3, the d-axis flux linkage changes nonlinearly with the d-axis current, whose curve is bent markedly at d-axis currents exceeding 10 A influenced by the saturation

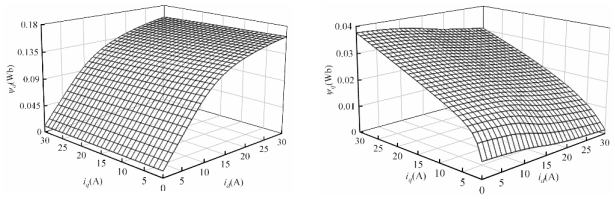

(a) d-axis flux linkage (b) q-axis flux linkage

FIGURE 3. Nonlinear flux linkages of the prototype SynRM.

TABLE 1. Identified model parameters.

self-saturation coefficients				cross-saturation coefficients	
α_d	0.0615	α_q	0.0071	k	0.0216
β_d	0.0013	β_q	0.00078	W	0.0020
γ_d	0.1498	γ_q	1.0321	V	0.2633
				V_1	0.0057
				κq	0.0758

TABLE 2. Parameters of SynRM prototype.

Parameters	Values	Parameters	Values
Rated Power (kw)	2	Rated Voltage (V)	42
Rated Speed (r·min^{-1})	1500	Rated Current (A)	35
Rated Torque (N·m)	12.7	Number of pole pairs	2
Stator resistance (Ω)	0.3	Moment of inertia (kg·m^{-2})	0.025

of magnetic circuit. Due to the influence of cross-coupling, the d-axis flux linkage also exhibits a slight decrease with increase in the q-axis current. The q-axis flux linkage also shows similar trends, which is affected more by the cross-coupling than the magnetic circuit saturation. Taking the FEA in Fig.3 as the reference data, the parameters in the model (12) are identified. Tab. 1 details the identification results.

IV. EXPERIMENTAL RESULTS

In order to verify the effectiveness of the proposed ANFTSMC-NDO algorithm in practical application, an experimental benchmark is established based on a SynRM prototype. The experimental benchmark including a dspace (ds1202), interface circuit board, SynRM, VSI drive, dc power supply, oscilloscope, torque sensor, load and its drive system, and personal computer is shown in Fig. 4. The basic parameters of the SynRM are shown in Table. 2 The tested SynRM is driven by a current-controlled VSI. The switching frequency of VSI is 10 kHz, and the dead-time is set to be 3.2 μs. The dc-link voltage of the VSI is set at 72 V and is provided by the dc power supply.

The design objective of the system is to track various reference commands robustly with the novel proposed ANFTSMC-NDO method. The speed response experiment under a constant load and the load experiment under a constant speed were implemented. The performance of the proposed ANFTSMC-NDO method and NTSMC method are compared in two experiments. The two types of experiments are named Experiment I and Experiment II respectively. In Experiment I, the speed step responses experiment results

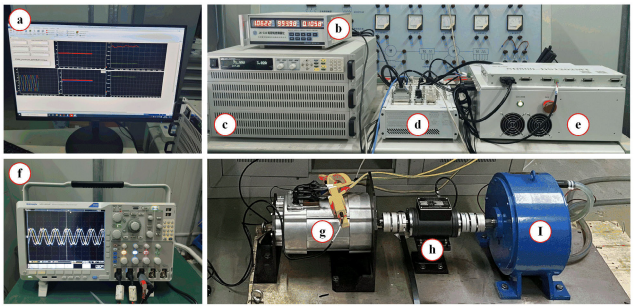

FIGURE 4. Experimental platform of SynRM prototype: (a) PC with software of dSPACE ControlDesk; (b) Torquemeter; (c) 9 kW DC power supply; (d) MicroLabBox dSPACE ds1202; (e) Customized three-phase inverter; (f) Oscilloscope; (g) 2-kW SynRM prototype with resolver; (h) Torque sensor; (I) Hysteresis brake.

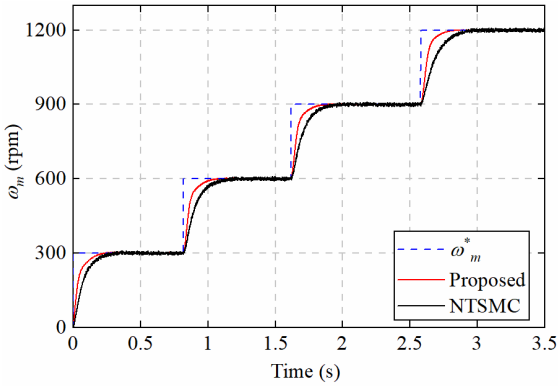

FIGURE 5. Experiment I, speed tracking comparison.

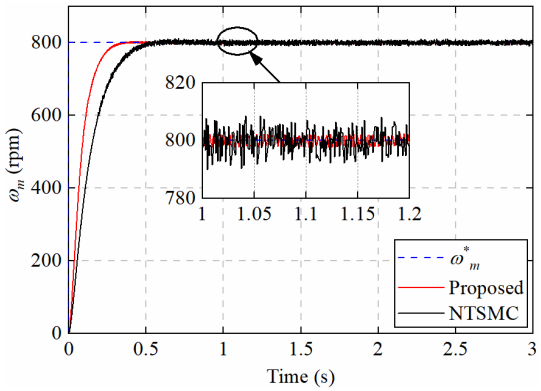

FIGURE 6. Experiment I, speed step responses.

are shown in Fig. 5 and Fig. 6. In Experiment II, the experimental results of the dynamic response during the loading process are shown in Figs. 7-9. To evaluate the performance of the two methods, the speed tracking error e_ω, the maximum speed tracking error $S_{\max}$, the average speed tracking error S_{av}, and the standard deviation of speed tracking error are defined as [30]:

$$e_\omega(n) = \omega_m^*(n) - \omega_m(n) \tag{49}$$

$$S_{\max} = \max_{t_n}(|e_\omega(n)|) \tag{50}$$

$$S_{\text{av}} = \frac{\sum_{n=1}^{t_n}|e_\omega(n)|}{t_n} \tag{51}$$

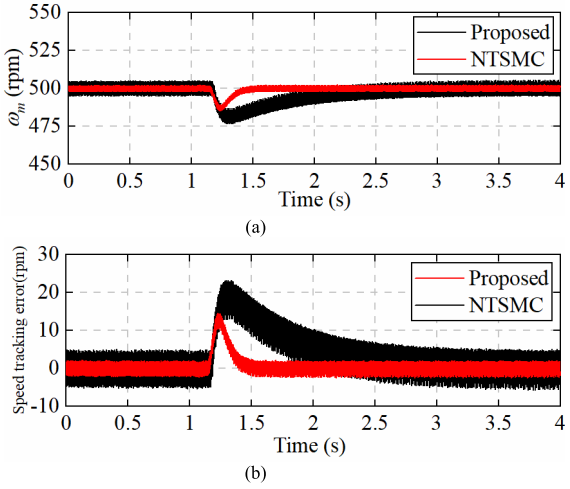

FIGURE 7. Speed tracking in case 1. (a) Speed response comparison. (b) Speed tracking error comparison.

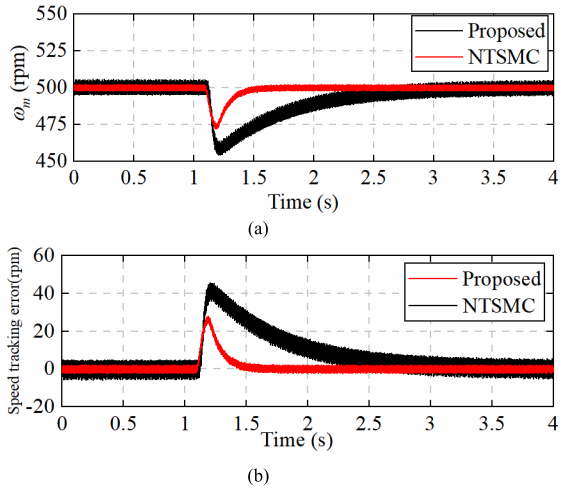

FIGURE 8. Speed tracking in case 2. (a) Speed response comparison. (b) Speed tracking error comparison.

TABLE 3. Comparison of the speed responses time.

	Proposed	NTSMC
0→300 rpm	0.221s	0.291s
300 rpm→600 rpm	0.225s	0.296s
600 rpm→900 rpm	0.228s	0.299s
900 rpm→1200 rpm	0.232s	0.333s
Average time	0.227s	0.305s
standard deviation	0.004s	0.017s

$$S_{\mathrm{sd}} = \sqrt{\frac{\sum_{n=1}^{t_n} \left(|e_\omega(n)| - S_{\mathrm{av}}\right)^2}{t_n}} \tag{52}$$

where t_n is the total number of iterations.

Fig. 5 compares the response performance of the proposed ANFTSMC-NDO method and NTSMC method during the ascent of the reference speed from 0 rpm to 1200 rpm with 300 rpm as the step. Compared with the NTSMC, the proposed method spends less time to reach the step speed command during the ascending process.

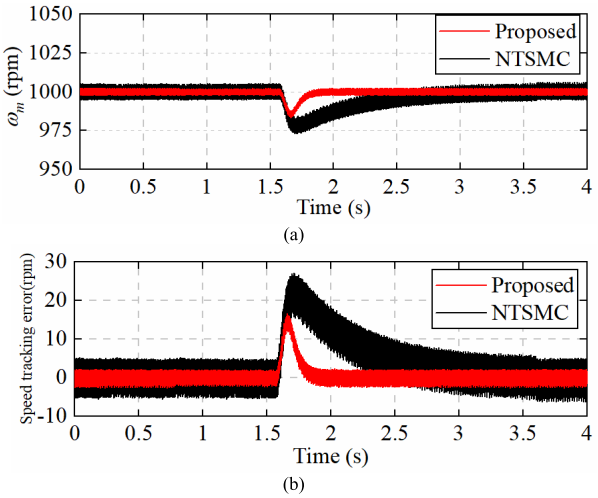

FIGURE 9. Speed tracking in case 3. (a) Speed response comparison. (b) Speed tracking error comparison.

TABLE 4. Scheme description of experiment II.

	Speed command (rpm)	Load torque (Nm)	Loading time (s)
Case1	500	1→3N	1.3
Case2	500	3→7N	1.2
Case3	1000	1→3N	1.6
Case4	1000	3→7N	0.8

Compared with NTSMC, the proposed method takes less time to reach the step speed command during the ascending process. In the steady state, the speed pulsation of the proposed method is smaller. The speed adjustment time during the experiment is compared in Table 3. In terms of average adjustment time, the proposed algorithm is 25.7% less than NTSMC. It can be seen from the comparison of the standard deviation of the adjustment time that the proposed algorithm has better robustness under the same step reference speed.

Fig. 6 shows the comparison of the step response when the 800rpm acceleration command is received. As shown in this Fig, when the speed command is given, the proposed ANFTSMC-NDO method spends less time to reach the command speed than NTSMC method. In steady state, the proposed method has less speed chattering.

In experiment II, sudden loads at constant speed are implemented to further verify the control performance under different loads. The experiment is divided into four cases, the load torque of two grades is suddenly applied under the reference speed command 500 rpm and 1000 rpm respectively. The scheme of experiment II is summarized in Table 4.

The experimental results of Case1 to Case4 are shown in Fig. 7 to Fig. 10. Under the 500 rpm reference speed command, the speed adjustment performance during the loading process is shown in Fig. 7(a), and Fig. 7(b) shows the comparison of the tracking error during the speed adjustment process. The results of other experiments are presented in a similar way to Case 1. In order to facilitate statistical analysis, the time spent in the four experiments is 4s.

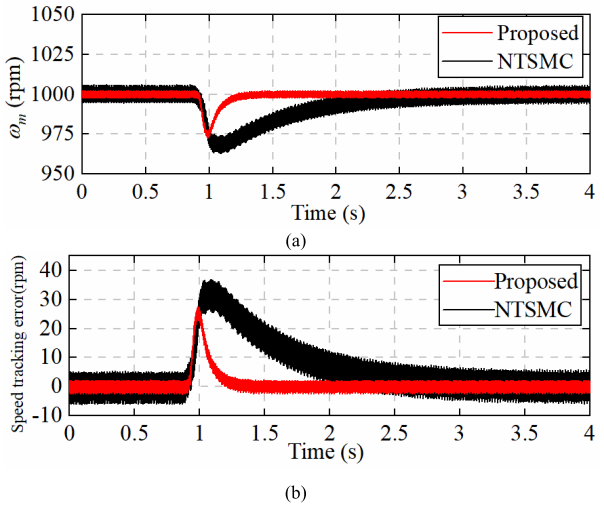

FIGURE 10. Speed tracking in case 4. (a) Speed response comparison. (b) Speed tracking error comparison.

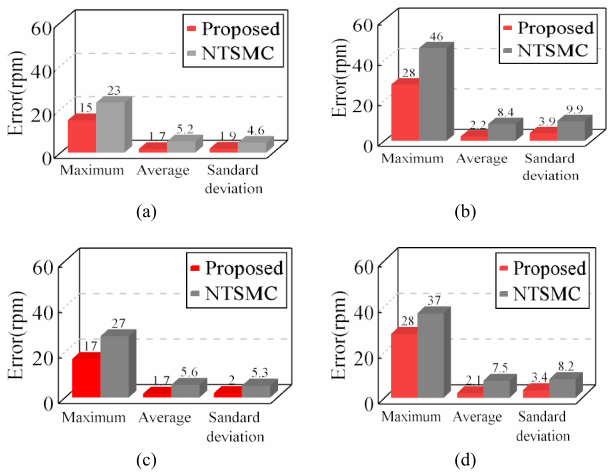

FIGURE 11. Performance evaluation. (a) Case1. (b) Case2. (c) Case3. (d) Case4.

In terms of dynamic response, the adjustment time of the proposed method is: 0.33s in case 1, 0.34s in case 2, 0.36s in case 3, and 0.39s in case 4, as shown in Fig. 7 to Fig. 10. The adjustment time spent by the NTSMC method in the four cases exceeds the time spent in the proposed method under the same conditions. From the experimental results, it can be intuitively observed that the proposed ANFTSMC-NDO method is better than NTSMC in dynamic performance. To further evaluate the control performance of the two methods. According to (50)-(52), the speed tracking error of the experimental results of the four cases are analyzed. The performance evaluation results of the two control methods based on the speed tracking error measurement are shown in Fig. 11.

As shown in Fig. 11, because the proposed ANFTSMC-NDO method has a powerful total disturbance compensation capability, its maximum tracking error is lower than the NTSM method in all four cases. On the other hand, in the comparison of the average tracking error and the standard deviation, the proposed ANFTSMC-NDO method is better than the NTSMC method. In other words, the A method has

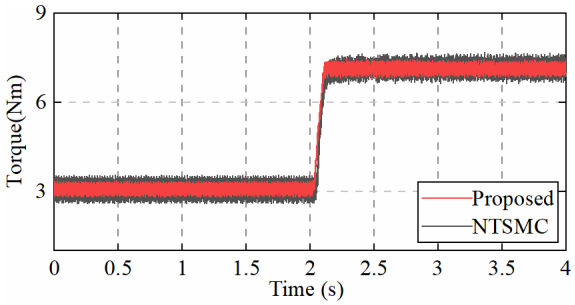

FIGURE 12. Output value of torque.

smaller speed pulsation during adjustment process and in steady state. Fig. 12 shows the torque curve of the proposed ANFTSMC-NDO method and the NTSMC method when the system is loaded at 2s. In steady state, the ANFTSMC-NDO method had less chattering than that of NTSMC scheme.

Based on the above experimental results, the proposed method has more satisfactory comprehensive performance than NTSMC. By using the proposed AERL, the steady-state velocity pulsation is significantly improved. In addition, the proposed method has ideal adjustment time and speed tracking capabilities during the loading process.

V. CONCLUSION

In this article, a novel control design based on ANFTSMC-NDO is proposed for the SynRM drive system. A non-singular sliding mode control law with adaptive gain arrival law and nonlinear disturbance observer has been developed to adjust the lumped uncertainty online to generate current loop commands. In addition, the time-varying parameters and controller parameters of SynRM are estimated online by the proposed analytical magnetic model. By implementing tracking experiments on different speed reference trajectories and different load conditions, the proposed ANFTSMC-NDO control scheme shows satisfactory speed control performance and robustness.

REFERENCES

[1] N. G. Ozcelik, U. E. Dogru, M. Imeryuz, and L. T. Ergene, "Synchronous reluctance motor vs. induction motor at low-power industrial applications: Design and comparison," *Energies*, vol. 12, no. 11, p. 2190, Jun. 2019.

[2] Y. Bao, M. Degano, S. Wang, L. Chuan, H. Zhang, Z. Xu, and C. Gerada, "A novel concept of ribless synchronous reluctance motor for enhanced torque capability," *IEEE Trans. Ind. Electron.*, vol. 67, no. 4, pp. 2553–2563, Apr. 2020.

[3] L. Ortombina, F. Tinazzi, and M. Zigliotto, "Adaptive maximum torque per ampere control of synchronous reluctance motors by radial basis function networks," *IEEE J. Emerg. Sel. Topics Power Electron.*, vol. 7, no. 4, pp. 2531–2539, Dec. 2019.

[4] F.-J. Lin, M.-S. Huang, S.-G. Chen, and C.-W. Hsu, "Intelligent maximum torque per ampere tracking control of synchronous reluctance motor using recurrent legendre fuzzy neural network," *IEEE Trans. Power Electron.*, vol. 34, no. 12, pp. 12080–12094, Dec. 2019.

[5] S. Yamamoto, H. Hirahara, J. B. Adawey, T. Ara, and K. Matsuse, "Maximum efficiency drives of synchronous reluctance motors by a novel loss minimization controller with inductance estimator," *IEEE Trans. Ind. Appl.*, vol. 49, no. 6, pp. 2543–2551, Nov. 2013.

[6] J. Bonifacio and R. M. Kennel, "On considering saturation and cross-coupling effects for copper loss minimization on highly anisotropic synchronous machines," *IEEE Trans. Ind. Appl.*, vol. 54, no. 5, pp. 4177–4185, Sep. 2018.

[7] H.-S. Kim, Y. Lee, S.-K. Sul, J. Yu, and J. Oh, "Online MTPA control of IPMSM based on robust numerical optimization technique," *IEEE Trans. Ind. Appl.*, vol. 55, no. 4, pp. 3736–3746, Jul. 2019.

[8] R. Antonello, M. Carraro, and M. Zigliotto, "Maximum-torque-per-ampere operation of anisotropic synchronous permanent-magnet motors based on extremum seeking control," *IEEE Trans. Ind. Electron.*, vol. 61, no. 9, pp. 5086–5093, Sep. 2014.

[9] T. Sun, J. Wang, and X. Chen, "Maximum torque per ampere (MTPA) control for interior permanent magnet synchronous machine drives based on virtual signal injection," *IEEE Trans. Power Electron.*, vol. 30, no. 9, pp. 5036–5045, Sep. 2015.

[10] G. Gallegos-Lopez, F. S. Gunawan, and J. E. Walters, "Optimum torque control of permanent-magnet AC machines in the field-weakened region," *IEEE Trans. Ind. Appl.*, vol. 41, no. 4, pp. 1020–1028, Jul. 2005.

[11] A. Consoli, G. Scarcella, G. Scelba, and A. Testa, "Steady-state and transient operation of IPMSMs under maximum-torque-per-ampere control," *IEEE Trans. Ind. Appl.*, vol. 46, no. 1, pp. 121–129, Jan./Feb. 2010.

[12] Z. Qu, T. Tuovinen, and M. Hinkkanen, "Inclusion of magnetic saturation in dynamic models of synchronous reluctance motors," in *Proc. 20th Int. Conf. Electr. Mach.*, Sep. 2012, pp. 994–1000.

[13] S. Li, M. Zhou, and X. Yu, "Design and implementation of terminal sliding mode control method for PMSM speed regulation system," *IEEE Trans. Ind. Informat.*, vol. 9, no. 4, pp. 1879–1891, Nov. 2013.

[14] Y. Feng, J. Zheng, X. Yu, and N. Vu Truong, "Hybrid terminal sliding-mode observer design method for a permanent-magnet synchronous motor control system," *IEEE Trans. Ind. Electron.*, vol. 56, no. 9, pp. 3424–3431, Sep. 2009.

[15] K. Rajagopal, F. Nazarimehr, A. Karthikeyan, A. Srinivasan, and S. Jafari, "Fractional order synchronous reluctance motor: Analysis, chaos control and FPGA implementation," *Asian J. Control*, vol. 20, no. 5, pp. 1979–1993, Sep. 2018.

[16] K. Zhao, T. Yin, C. Zhang, J. He, X. Li, Y. Chen, R. Zhou, and A. Leng, "Robust model-free nonsingular terminal sliding mode control for PMSM demagnetization fault," *IEEE Access*, vol. 7, pp. 15737–15748, Jan. 2019.

[17] H. Huang, Q. Tu, C. Jiang, and M. Pan, "Nonsingular terminal sliding mode control based on sensor-cloud system for permanent magnet in-wheel motor," *IEEE Access*, vol. 8, pp. 140399–140410, Jul. 2020.

[18] S. Chen, W. Liu, and H. Huang, "Nonsingular fast terminal sliding mode tracking control for a class of uncertain nonlinear systems," *J. Control Sci. Eng.*, vol. 2019, pp. 1–17, May 2019.

[19] S. Wu, X. Su, and K. Wang, "Time-dependent global nonsingular fixed-time terminal sliding mode control-based speed tracking of permanent magnet synchronous motor," *IEEE Access*, vol. 8, pp. 186408–186420, Oct. 2020.

[20] H. Eldeeb, C. M. Hackl, L. Horlbeck, and J. Kullick, "A unified theory for optimal feedforward torque control of anisotropic synchronous machines," *Int. J. Control*, vol. 91, no. 10, pp. 2273–2302, Jul. 2017.

[21] S. Wiedemann, S. Hall, R. M. Kennel, and M. Alakula, "Dynamic testing characterization of a synchronous reluctance machine," *IEEE Trans. Ind. Appl.*, vol. 54, no. 2, pp. 1370–1378, Mar. 2018.

[22] S. M. Ferdous, P. Garcia, M. A. M. Oninda, and M. A. Hoque, "MTPA and field weakening control of synchronous reluctance motor," in *Proc. 9th Int. Conf. Electr. Comput. Eng. (ICECE)*, Dec. 2016, pp. 598–601.

[23] A. Varatharajan, S. Cruz, H. Hadla, and F. Briz, "Predictive torque control of SynRM drives with online MTPA trajectory tracking and inductances estimation," in *Proc. IEEE Int. Electric Mach. Drives Conf. (IEMDC)*, May 2017, pp. 1–7.

[24] M. N. Ibrahim, P. Sergeant, and E. M. Rashad, "Relevance of including saturation and position dependence in the inductances for accurate dynamic modeling and control of SynRMs," *IEEE Trans. Ind. Appl.*, vol. 53, no. 1, pp. 151–160, Jan. 2017.

[25] C. J. Fallaha, M. Saad, H. Y. Kanaan, and K. Al-Haddad, "Sliding-mode robot control with exponential reaching law," *IEEE Trans. Ind. Electron.*, vol. 58, no. 2, pp. 600–610, Feb. 2011.

[26] G. S. Rajanna and H. N. Nagaraj, "Comparison between sigmoid variable reaching law and exponential reaching law for sliding mode controlled DC-DC buck converter," in *Proc. Int. Conf. Power, Energy Control (ICPEC)*, Feb. 2013, pp. 316–319.

[27] K. B. Devika and S. Thomas, "Improved sliding mode controller performance through power rate exponential reaching law," in *Proc. 2nd Int. Conf. Electr., Comput. Commun. Technol. (ICECCT)*, Feb. 2017, pp. 1–7.

[28] G. Arechavaleta, A. Morales-Diaz, H. M. Perez-Villeda, and M. Castelan, "Hierarchical task-based control of multirobot systems with terminal attractors," *IEEE Trans. Control Syst. Technol.*, vol. 25, no. 1, pp. 334–341, Jan. 2017.

[29] W.-H. Chen, J. Yang, and Z. Zhao, "Robust control of uncertain nonlinear systems: A nonlinear DOBC approach," *J. Dyn. Syst., Meas., Control*, vol. 138, no. 7, pp. 823–828, May 2016.

[30] F.-J. Lin, M.-S. Huang, S.-G. Chen, C.-W. Hsu, and C.-H. Liang, "Adaptive backstepping control for synchronous reluctance motor based on intelligent current angle control," *IEEE Trans. Power Electron.*, vol. 35, no. 7, pp. 7465–7479, Jul. 2020.

LINJIE REN received the B.S. degree in industrial automation and the M.S. degree in control theory and control engineering from Lanzhou Jiaotong University, Lanzhou, China, in 2011 and 2017, respectively. He is currently pursuing the Ph.D. degree with Tongji University. His current research interests include control with applications to mechatronic systems and power quality analysis and control.

GUOBIN LIN received the B.S. degree in electric machine from Zhejiang University, Hangzhou, China, in 1986, and the M.S. degree in electrical engineering from Southwest Jiaotong University, Chengdu, China, in 1989.

He is currently a Professor and the Deputy Director of National Maglev Transportation Engineering Technology Research Center, Tongji University, Shanghai, China. His research interests include maglev vehicle and linear drive research.

YUANZHE ZHAO received the B.S. degree in electrical engineering and automation and the Ph.D. degree in power system and automation from Southwest Jiaotong University, Chengdu, China, in 2009 and 2016, respectively.

He currently holds a postdoctoral position with the College of Transportation Engineering and the National Maglev Transportation Engineering Technology Research Center, Shanghai, China. His research interests include power quality analysis and control, harmonic analysis, and control of electrical drives.

ZHIMING LIAO received the B.S. degree in mechanical design and manufacturing from the Wuhan University of Hydraulic and Electrical Engineering, Wuhan, China, in 1995, and the M.S. degree in power electronics and electrical drives from Southwest Jiaotong University, Chendu, China, in 2003. He is currently a Senior Engineer with the National Maglev Transportation Engineering Research and Development Center, Tongji University, Shanghai, China. His main research interests include linear motor design, motor control, and power supply system of maglev train.

FEI PENG received the B.S. degree in electronic engineering and automation and the Ph.D. degree in power system and automation from Southwest Jiaotong University, Chengdu, China, in 2009 and 2014, respectively. He is currently working with College of Electrical Engineering, Qingdao University, Qingdao, China. His research interest includes levitation control technology of maglev train.